energies

MDPI

*Article*

# Static and Dynamic Magnetic Pull in Modular Spoke-Type Permanent Magnet Motors

**Shaonan Sun, Guihong Feng *, Yan Li and Bingyi Zhang**

School of Electrical Engineering, Shenyang University of Technology, Shenyang 110870, China; mytcdssn@163.com (S.S.)
* Correspondence: fenggh@sut.edu.cn; Tel.: +86-13591690366

**Abstract:** This work studied the static magnetic pull of a modular spoke-type permanent magnet motor (MSTPMM) with no rotor eccentricity during the motor's final assembly process and its dynamic magnetic pull during different motor operating states. A new final assembly scheme was proposed to significantly reduce the static magnetic pull during the final assembly process of the motor. The methods required to reduce the unbalanced radial magnetic pull of the whole stator, which is caused by partial stator module operation, were also studied. Firstly, the structure of the MSTPMM was examined. The static magnetic pull that occurred with the implementation of the two motor final assembly methods was studied in order to prove the effectiveness of reducing the maximum static magnetic pull. Moreover, the maximum magnetic pull during the assembly process was also observed. Then, the dynamic magnetic pull was studied with different motor operating states: no load, on load, and partial stator module operation. To solve the unbalanced radial magnetic pull of the whole stator, which is caused by partial stator module operation, methods of changing the angle between the stator current vector and the q axis ($\Psi$) or the d axis current ($i_d$) were also studied.

**Keywords:** static magnetic pull; dynamic magnetic pull; modular spoke-type permanent magnet motor (MSTPMM); final assembly



**Citation:** Sun, S.; Feng, G.; Li, Y.; Zhang, B. Static and Dynamic Magnetic Pull in Modular Spoke-Type Permanent Magnet Motors. *Energies* **2023**, *16*, 4078. https://doi.org/10.3390/en16104078

Academic Editor: Miguel Castilla

Received: 3 April 2023
Revised: 2 May 2023
Accepted: 11 May 2023
Published: 13 May 2023



## 1. Introduction

The spoke-type permanent magnet motor has been widely studied in home and vehicle appliances because it can concentrate flux and has a high torque density and potential magnet-saving capabilities [1–3]. The majority of studies have been mainly focused on the magnet shape [4–11], the analytical model [12,13] and the magnetic barrier, with different shapes and dimensions [14–21], for high-speed spoke-type permanent magnet motors. However, a study on the magnetic pull of modular stators or rotors for modular spoke-type permanent magnet motors has not yet been conducted.

In a modular spoke-type permanent magnet motor (MSTPMM), the modular stator and modular rotor are fixed separately. Therefore, the magnetic pull of the modular stator and rotor in the assembly process, as well as its operating states, need to be analyzed separately. In addition, the magnetic pull that mainly influences the motor's fixed structure and assembly positioning tooling mechanical strength consists of the following: the radial magnetic pull of one modular rotor core ($F_{rMR}$), the tangential magnetic pull of one modular rotor core ($F_{tMR}$), the radial magnetic pull of one modular stator core ($F_{rMS}$), the tangential magnetic pull of one modular stator core ($F_{tMS}$), the magnetic pull of one modular stator core ($F_S$), and the magnetic pull of the whole stator ($F_{WS}$).

This paper proposed two assembly schemes for MSTPMM; found the maximum static magnetic pull during motor final assembly process; and proposed a method to reduce the unbalanced radial magnetic pull of the whole stator, which was caused by part of the stator modules operating. This paper will be organized as follows. First, the structure and parameters of a modular spoke-type permanent magnet motor (MSTPMM) is introduced in

the second section. Two motor final assembly methods, which are suited to large-volume permanent magnet motors in order to reduce static magnetic pull, are proposed in Section 3. The static magnetic pulls that occurred following the implementation of the two motor final assembly methods are analyzed. In Section 4, the dynamic magnetic pulls are studied with different motor operating states: no load, on load, and partial stator module operation. Then, in Section 5, to solve the unbalanced radial magnetic pull of the whole stator, which is caused by partial stator module operation, the methods of changing the angle between the stator current vector and the q axis ($\Psi$) or the d axis current ($i_d$) are studied.

## 2. Structure of Non-Magnetic Supports for Spoke-Type Permanent Magnet Motor and Motor Parameters

A diagram of non-magnetic stainless-steel supports for an outer rotor modular spoke-type permanent magnet motor is shown in Figure 1.

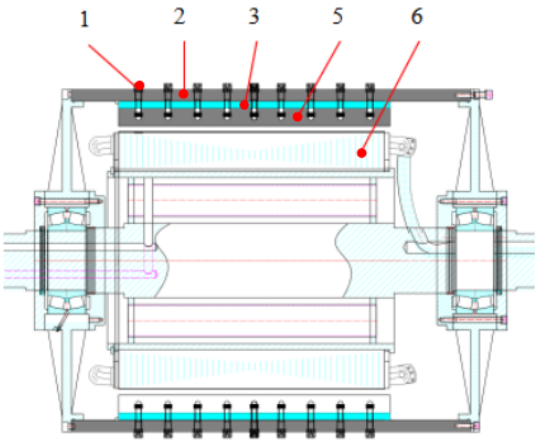


(**a**) Overall schematic diagram

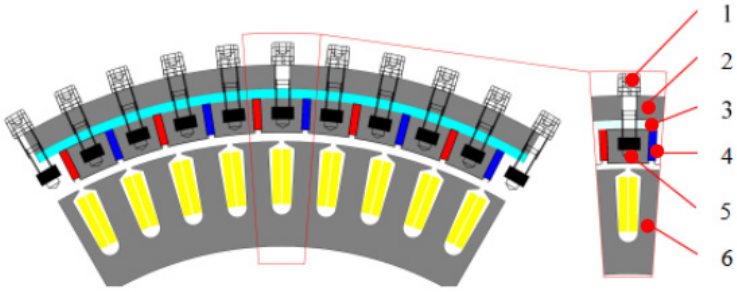


(**b**) Local schematic diagram

**Figure 1.** Diagram for the outer rotor of the MSTPMM. 1. Non-magnetic bolt; 2. outer rotor yoke; 3. non-magnetic stainless steel; 4. permanent magnet; 5. modular rotor core; and 6. modular stator core.

The coil layout of one modular stator (10 pole–12 slot) is shown in Figure 2, where the numbers are the stator tooth number, and the letters are the phase of the windings belong. The modular motor parameters are shown in Table 1. The stators and rotors are all modular, the number of modular stators is 6, and the number of modular rotors is 60.

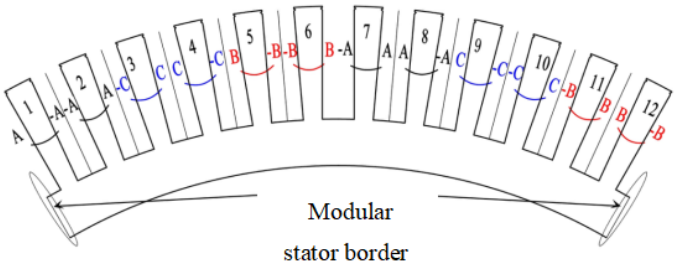


**Figure 2.** Coil layout of one modular stator.

**Table 1.** Main parameters of motor.

| Parameter | Values and Units |
|---|---|
| Rated power | 160 kW |
| Rated voltage | 1140 V |
| Rated speed | 30 rpm |
| Rated torque | 50,933 N·m |
| Rated frequency | 15 Hz |
| Stack length ($L_a$) | 1000 mm |
| Stator outer diameter ($D_1$) | 1149.4 mm |
| Thickness of stator yoke | 40 mm |
| Air gap ($g_1$) | 2.3 mm |
| Magnet magnetization direction dimension ($h_m$) | 10 mm |
| Magnet width ($b_m$) | 40 mm |
| Thickness of non-magnetic stainless steel ($h_3$) | 30 mm |
| Number of stator slots ($z$)/rotor pole pairs ($p$) | 72/30 |
| Iron core material | DW470_50 |
| PM material | N42UH |
| Number of modular stators | 6 |
| Number of modular rotors | 60 |

## 3. Static Magnetic Pull in Different Magnet Assembly Processes

### *3.1. The Description of the Motor Assembly Scheme*

This section proposes two final motor assembly schemes. The final assembly process of Scheme A is shown in Figure 3a and is divided into three steps:

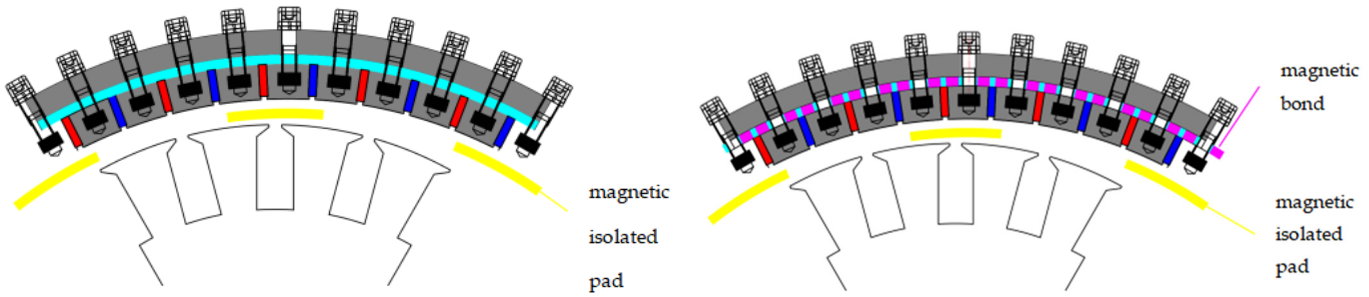


(**a**) Scheme A (**b**) Scheme B

**Figure 3.** Schematic diagram of the motor assembly scheme.

(Step A1) The stator part and rotor part with magnets are independently assembled.

(Step A2) Between the stator and rotor, the magnetic isolated pads are inserted equidistributionally in the circle direction. Then, the stator and rotor are assembled together.

(Step A3) The magnetic isolated pads are removed through assembly holes at the end closure. The hole is shown in Figure 4.

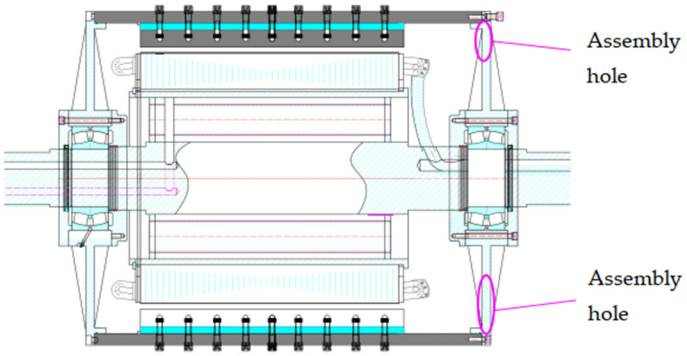


**Figure 4.** Schematic diagram of the assembly hole location.

The final assembly process of Scheme B is shown in Figure 3b and is divided into three steps:

(Step B1) The stator part and rotor part with magnets are independently assembled. During the rotor part assembly process, the magnetic bonds assembly process must take place before the magnets are assembled.

(Step B2) Between the stators and rotors, the magnetic isolated pads are inserted equidistributionally in the circle direction. Then, the stator and rotor are assembled together.

(Step B3) The magnetic bonds and magnetic isolated pads are removed through assembly holes at the end closure. The hole is shown in Figure 4.

### *3.2. The Static Magnetic Pull Description of Motor Assembly Scheme A*

$N_{rotor\_left}$ is the number of adjacent filled-groove magnets, which are on the left of the analyzed modular rotor core. $N_{rotor\_right}$ is the number of adjacent filled-groove magnets, which are on the right of the analyzed modular rotor core. The diagrammatic sketch of $N_{rotor\_left}$ and $N_{rotor\_right}$ is shown in Figure 5.

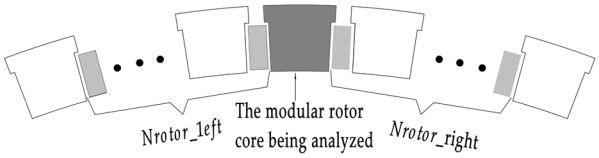


**Figure 5.** The diagrammatic sketch of $N_{rotor\_left}$ and $N_{rotor\_right}$.

The local enlarged rotor schematic of rotor core A is shown in Figure 6, into which magnet grooves 1 and 2 inserted magnets, where the numbers are the magnetic grooves number, the letters are the rotor core letter. The corresponding magnetic flux distribution of Steps A1 and B1 is shown in Figure 7, where, $\Phi_r$, $\Phi_m$, $\Phi_{magA1}$, and $\Phi_{magA2}$ are the remanent magnet flux, magnet leakage flux, air-gap flux on the left of core A, and air-gap flux on the right of core A, respectively; $\Phi_{gA11}$, $\Phi_{gB11}$, and $\Phi_{gC11}$ are the core magnetic flux on the bottom of core A, B, and C near the air gap, respectively; and $\Phi_{gA21}$, $\Phi_{gB21}$, and $\Phi_{gC21}$ are the core magnetic flux on top of core A, B, and C near the non-magnetic stainless steel, respectively. $\Phi_{b11}$ and $\Phi_{b12}$ are the leakage magnetic flux near the air gap.

The basic formula of electromagnetic suction is shown in expression (1).

$$F = \frac{\phi^2}{2\mu_0 b L_{ef}} \tag{1}$$

where $\Phi$ is air-gap flux, $\mu_0$ is the magnetoconductivity of air, $b$ is magnetic field cross section width, and $L_{ef}$ is the length of stator core.

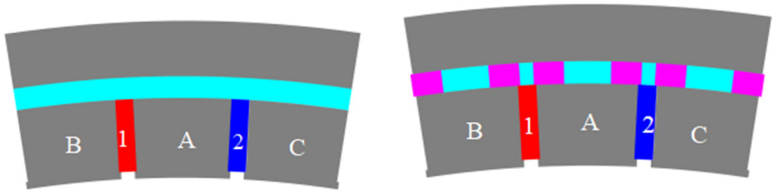


(**a**) Scheme A (**b**) Scheme B

**Figure 6.** The local enlarged rotor schematic of rotor core A (with inserted magnets via magnet grooves 1 and 2).

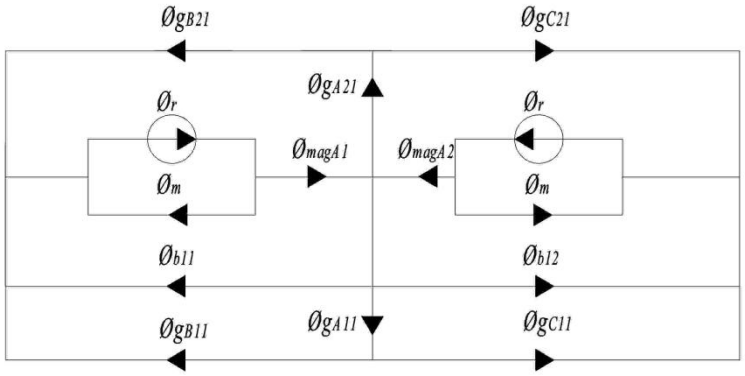


**Figure 7.** Schematic diagram of magnetic flux distribution.

The tangential magnetic pull of core A ($F_{tMRA}$) and the radial magnetic pull of core A ($F_{rMRA}$) are shown in expression (2).

$$\begin{cases} F_{tMRA} = \frac{(\phi_{magA1}{}^2 - \phi_{magA2}{}^2)}{2\mu_0 b_m L_{ef}} + \frac{(\phi_{b11}{}^2 - \phi_{b12}{}^2)}{2\mu_0 b_1 L_{ef}} \\ F_{rMRA} = \frac{\phi_{gA11}{}^2}{2\mu_0 b_{A1} L_{ef}} - \frac{\phi_{gA21}{}^2}{2\mu_0 b_{A2} L_{ef}} \end{cases} \quad (2)$$

where $b_m$ is the width of magnet, $b_1$ is the radial length of the magnetic isolated barrier near the air gap, $b_{A1}$ is the bottom arc length of core A near the air gap, and $b_{A2}$ is the top arc length of core A near the non-magnetic stainless steel.

The magnetic pull is simulated by finite element simulation software (Ansoft Maxwell 16). In order to facilitate the simulation, the following assumptions were made:

(1) The magnetic pull caused by axial end flux is ignored, and 2D simulation is used.
(2) The value of magnetic pull shown in the below figures is the maximum magnetic pull among the whole mechanical rotation circle.
(3) The eccentricities of motor and inconsistencies of permanent magnet performance are not considered.

The simulation tangential magnetic pull of one modular rotor core ($F_{tMR}$) and the radial magnetic pull of one modular rotor core ($F_{rMR}$) in the process of Scheme A, Step A1 are shown in Figure 8. The magnetic pull of the rotors and stators with different magnetic isolated pad thicknesses in the process of Scheme A, Step A2 are shown in Figure 9. The analyzed modular stator shown in Figure 9b is the one modular stator that had a minimum air-gap distance with the rotor. When the thickness of the magnetic isolated pad is 2.3 mm, then the magnetic pull of the stator and rotor in Step A3 are the same as the magnetic pull of the stator and rotor in Step A2.

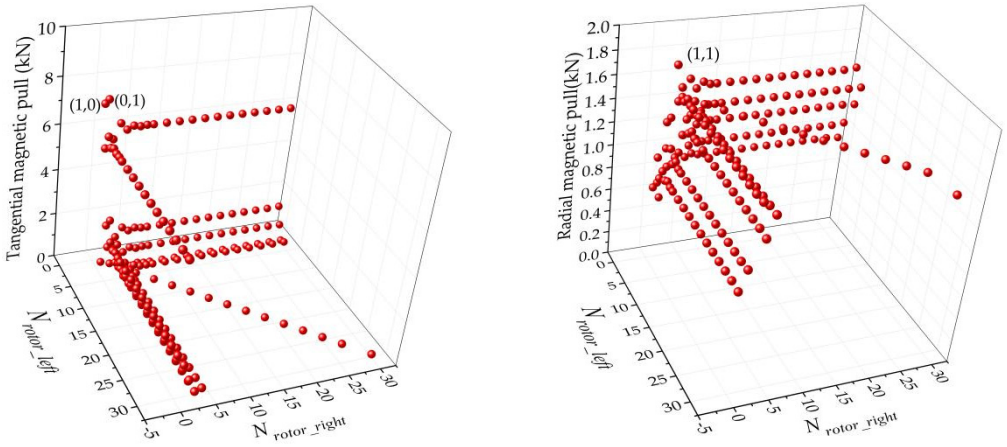


(**a**) Tangential magnetic pull ($F_{tMR}$) (**b**) Radial magnetic pull ($F_{rMR}$)

**Figure 8.** Magnetic pull of one modular rotor core in the Scheme A, Step A1 process.

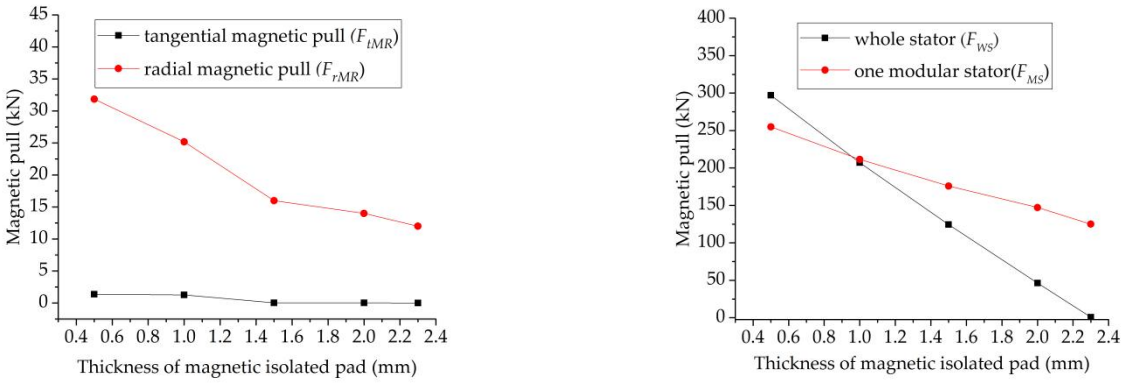


(**a**) Magnetic pull of one modular rotor (**b**) Magnetic pull of one modular stator and whole stator

**Figure 9.** Magnetic pull of rotor and stator with different magnetic isolated pad thickness in the Scheme A, Step A2 process.

Figures 8 and 9 show that in the Scheme A process:

(1) When the left or right adjacent magnet grooves insert magnets, that is, when ($N_{rotor\_left}$, $N_{rotor\_right}$) = (1, 0) or (0, 1) as in Step A1, the tangential magnetic pull of one modular rotor core ($F_{tMR}$) is at the maximum, as shown in Figure 8a.

(2) The radial magnetic pull of one modular rotor core ($F_{rMR}$) is at the maximum when the assembly process is in A2, which is shown in Figure 9a.

(3) Through increasing the thickness of the magnetic isolated pad, $F_{rMR}$, $F_{WS}$, and $F_{MS}$ can be reduced significantly.

### *3.3. The Static Magnetic Pull Description of Motor Assembly Scheme B*

The simulation magnetic pull of one modular rotor in the process of Scheme B, Step B1 is shown in Figure 10. When the radian of the magnetic bond is $\theta^\circ$, the magnetic pull of the whole stator ($F_{WS}$) is assumed to be $F_{WS}(\theta^\circ)$, and the magnetic pull of modular stator ($F_{MS}$) is assumed to be $F_{MS}(\theta^\circ)$. Then, the reduction percent of the whole stator magnetic pull is assumed to be $[F_{WS}(0^\circ) - F_{WS}(\theta^\circ)]/F_{WS}(0^\circ)$; the reduction percent of the modular stator magnetic pull is assumed to be $[F_{MS}(0^\circ) - F_{MS}(\theta^\circ)]/F_{MS}(0^\circ)$. The magnetic pull of one modular rotor and stator with different magnetic bond radians and magnetic isolated pad thicknesses during the process of Scheme B, Step B2 are shown in Figure 11, where the analyzed modular stator, shown in Figure 11e,f, has a minimum air-gap distance among all modular stators.

Figures 10 and 11 show that in the Scheme B process:

(1) When the left or right adjacent filled-groove magnets are ($N_{rotor\_left}$, $N_{rotor\_right}$) = (1, 0), or (0, 1), as in Step B1, then the tangential magnetic pull of one modular rotor core ($F_{tMR}$) is at the maximum. This is shown in Figure 10a–c.

(2) Through increasing the radian of the magnetic bond, the $F_{rMR}$, $F_{WS}$, and $F_{MS}$ can be smaller than what is found in Scheme A with the same magnetic isolated pad, especially when the magnetic isolated pad is thin. Figure 11d,e show that the value of $F_{WS}$ and $F_{MS}$ with 1.5° radian of magnetic bond can be reduced to 50% value of $F_{WS}$ and $F_{MS}$ without magnetic bond.

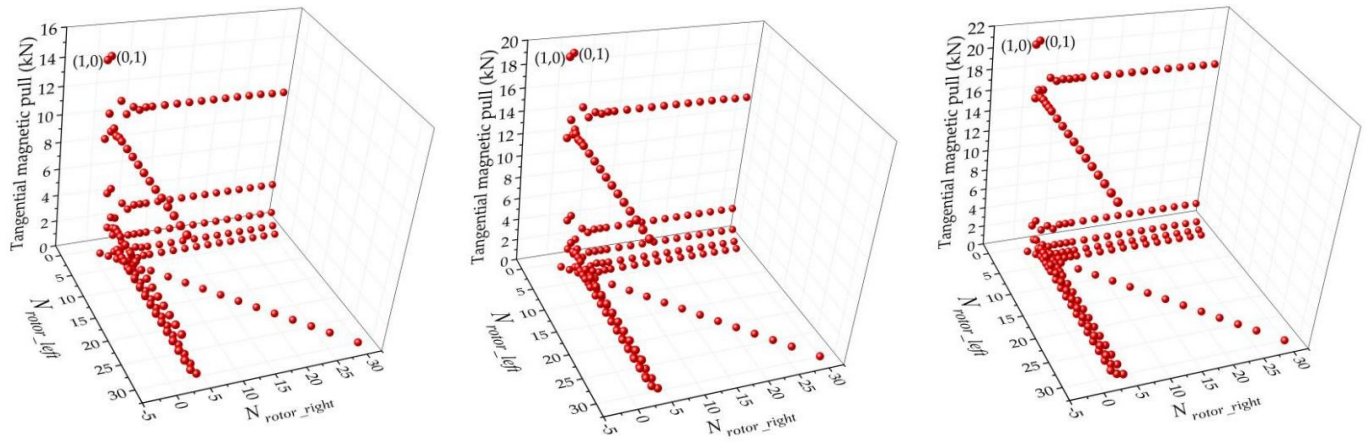


(**a**) Tangential magnetic pull ($F_{tMR}$) (radian of magnetic bond is 0.5°)

(**b**) Tangential magnetic pull ($F_{tMR}$) (radian of magnetic bond is 1°)

(**c**) Tangential magnetic pull ($F_{tMR}$) (radian of magnetic bond is 1.5°)

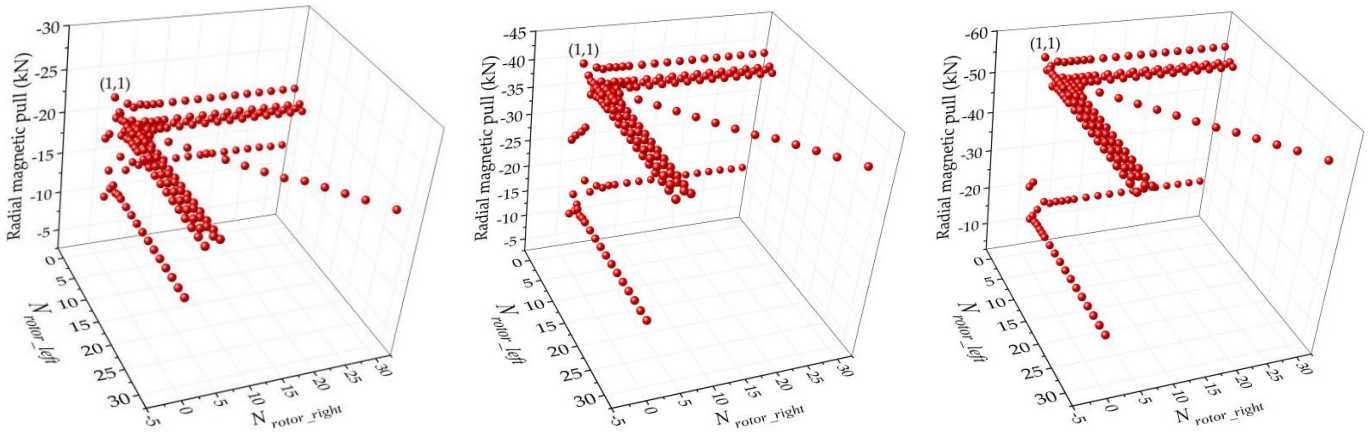


(**d**) Radial magnetic pull ($F_{rMR}$) (radian of magnetic bond is 0.5°)

(**e**) Radial magnetic pull ($F_{rMR}$) (radian of magnetic bond is 1°)

(**f**) Radial magnetic pull ($F_{rMR}$) (radian of magnetic bond is 1.5°)

**Figure 10.** Magnetic pull of one modular rotor core in the process of Scheme B, Step B1.

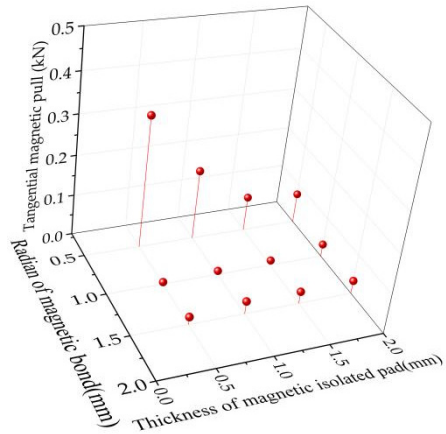


(**a**) Tangential magnetic pull of modular rotor ($F_{tMR}$)

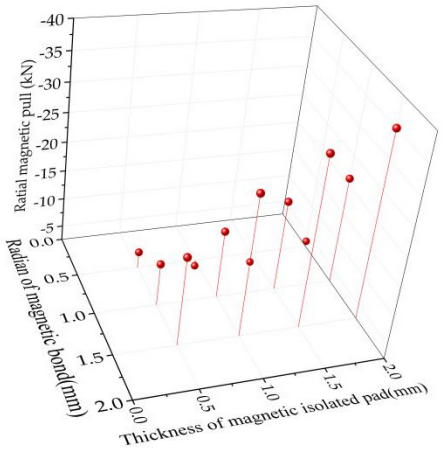


(**b**) Radial magnetic pull of modular rotor ($F_{rMR}$)

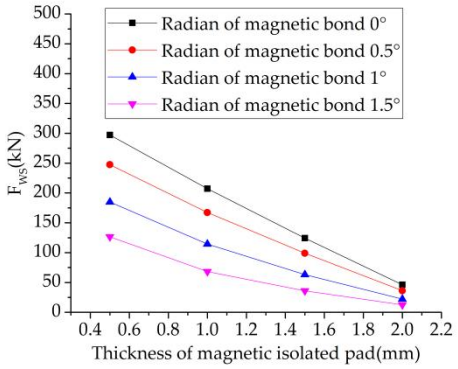


(**c**) Magnetic pull of whole stator ($F_{WS}$)

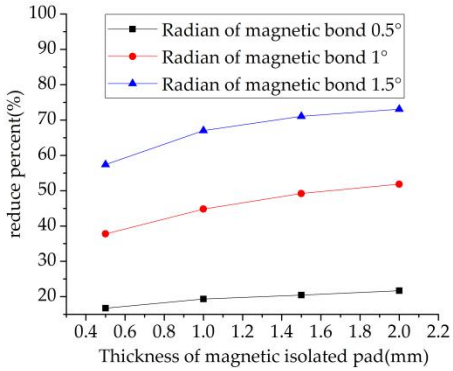


(**d**) The reduction percent of whole stator magnetic pull

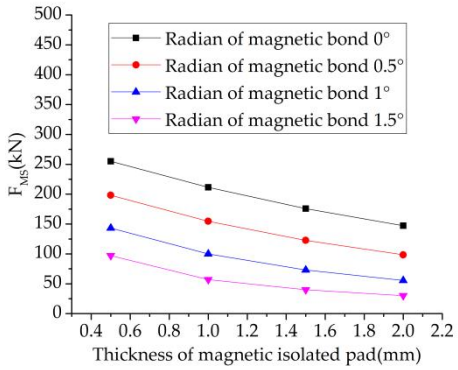


(**e**) Magnetic pull of modular stator ($F_{MS}$)

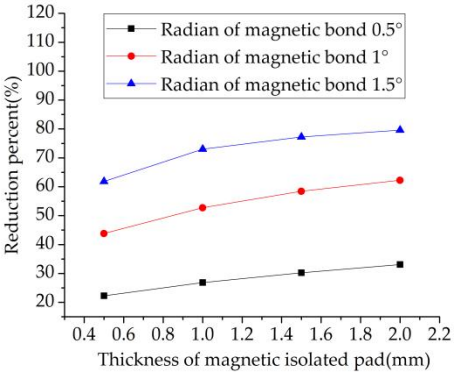


(**f**) The reduction percent of modular stator magnetic pull

**Figure 11.** The magnetic pull of one modular rotor and stator with different magnetic bond radians and magnetic isolated pad thicknesses during the Scheme B, Step B2 process.

## 4. Dynamic Magnetic Pull in Different Operating States

### *4.1. Full Stator Module Operation*

When the d axis current $i_d < 0$ or $i_d > 0$, then the stator current can influence the d axis magnetic field of the whole motor, which can then influence the magnetic pull of the rotor. The magnetic pull of the motor and rotor with different loads and $\Psi$ are shown in Figures 12 and 13, respectively. This is where the $\Psi$ is the angle between the stator current vector and the q axis, and $i_{whole.}$ is the whole stator phase current's effective value, which is where every stator module's phase current is $i_{whole}/6$.

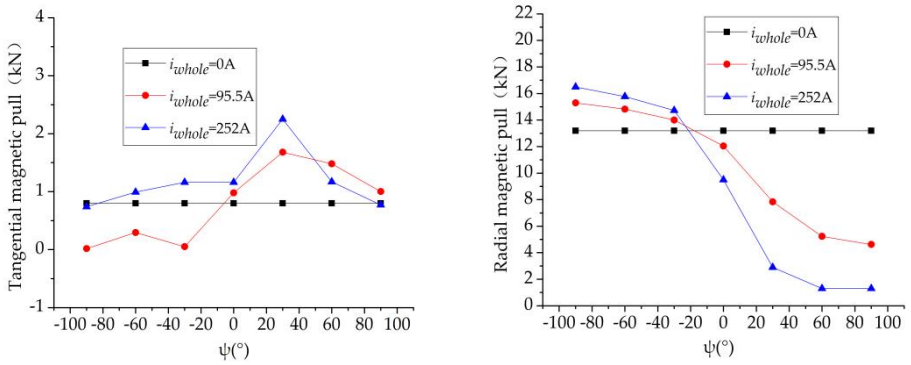


(**a**) Tangential magnetic pull ($F_{tMR}$) (**b**) Radial magnetic pull ($F_{rMR}$)

**Figure 12.** The magnetic pull of one modular rotor with different load currents and Ψ.

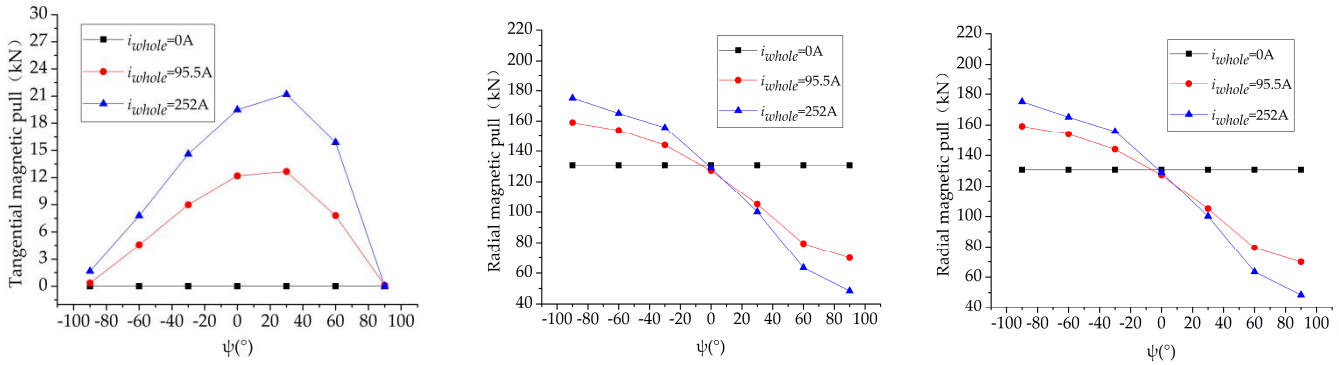


(**a**) Tangential magnetic pull of one modular stator ($F_{tMS}$)

(**b**) Radial magnetic pull of one modular stator ($F_{rMS}$)

(**c**) Magnetic pull of modular stator ($F_{MS}$)

**Figure 13.** The magnetic pull of the stator with different loads and Ψ.

Figures 12 and 13 show the following:

(1) Ψ mainly influences the $F_{rMR}$, $F_{WS}$, $F_{rMS}$, and $F_{MS}$. The influence degree is directly proportional to the magnitude of the stator current.

(2) When Ψ is close to −90° and the value of $i_{whole}$ is at the maximum, then $F_{rMR}$, $F_{MS}$, and $F_{rMS}$ can be at the maximum for different load currents and Ψ.

### *4.2. Partial Stator Module Operation*

The maximum magnetic pull of the modular rotor ($F_{tMR}$, $F_{rMR}$) and the modular stator's magnetic pull ($F_{tMS}$, $F_{rMS}$) were not influenced by the number of stator modules operating. Therefore, this section only shows the magnetic pull of the whole stator ($F_{WS}$), which is influenced by the number of operating stator modules (shown in Figure 14). Here, $i_m$ is the operating stator module phase current and the operating stator module that is adjacent to it.

Figure 14 shows the following:

(1) With the same number of adjacent stator modules operating, when Ψ is close to 90° and the value of $i_m$ is at the maximum, then the magnetic pull of the whole stator ($F_{WS}$) can be at the maximum;

(2) With the same current and Ψ, and when half of the stator is operating (i.e., the number of adjacent modular stators is three), then the magnetic pull of the stator ($F_{WS}$) can be at the maximum.

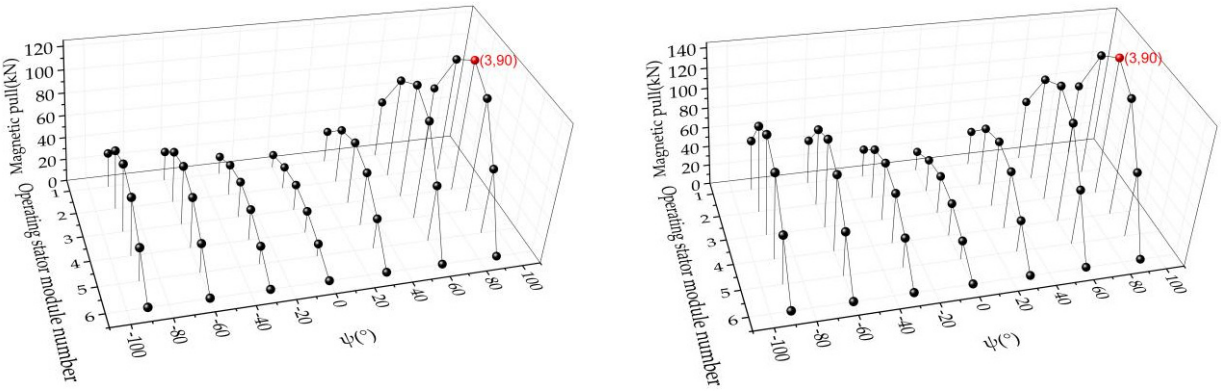


(**a**) $i_m$ = 15.9A (**b**) $i_m$ = 42A

**Figure 14.** The magnetic pull of the whole stator with different numbers of operating modular stators.

## 5. A Method for Reducing the Unbalanced Magnetic Pull of the Whole Stator

Section 4.2 shows that $\Psi$ or $i_d$ can significantly influence the magnetic pull of the stator ($F_{WS}$ and $F_{rMS}$) with the same stator current. Based on this conclusion, the way to reduce the unbalanced magnetic pull of the whole stator ($F_{WS}$) is proposed by a change in $\Psi$ or when the proportion of $i_d$ is in line with the stator current.

### *5.1. One Operating Modular Stator*

The modular stators are numbered from 1 to 6 (shown in Figure 15). Additionally, the corresponding current expressions are shown in (3), where $k$ = 1, 2, 3, 4, 5, 6 represents the stator number; $i_{d(k)}$ is the $d$ axis current of the stator module $k$; $i_{q(k)}$ is the $q$ axis current of the stator module $k$; $i_{A(k)}$, $i_{B(k)}$, and $i_{C(k)}$ are the three phases of the current of stator module $k$; and $\theta$ is the angle between the d axis of the rotor and the winding axis of A phase (electrical degree).

$$\begin{bmatrix} i_{d(\mathrm{k})} \\ i_{q(\mathrm{k})} \end{bmatrix} = \sqrt{\frac{2}{3}} \begin{bmatrix} \cos\theta & \cos(\theta - \frac{2\pi}{3}) & \cos(\theta + \frac{2\pi}{3}) \\ -\sin\theta & -\sin(\theta - \frac{2\pi}{3}) & -\sin(\theta + \frac{2\pi}{3}) \end{bmatrix} \begin{bmatrix} i_{A(k)} \\ i_{B(k)} \\ i_{C(k)} \end{bmatrix} \tag{3}$$

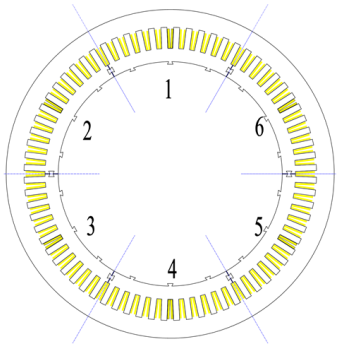


**Figure 15.** Diagrammatic sketch of the number of modular stators.

The radial magnetic pull of the whole stator ($F_{rWS}$), the load torque (T), the stator copper loss with a single modular stator operating ($\rho_{cu}$), and stator iron loss ($\rho_{fe}$) are shown in Figures 16 and 17.

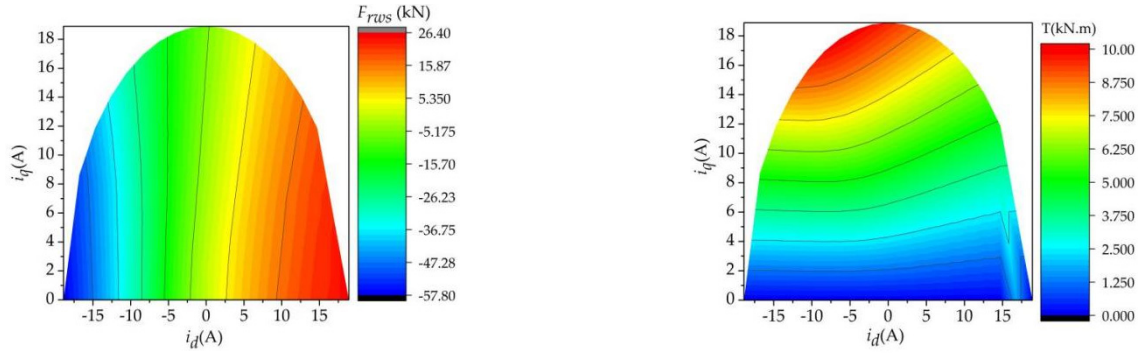


(**a**) Radial magnetic pull of the whole stator ($F_{rWS}$) (**b**) The load torque(T)

**Figure 16.** The radical magnetic pull ($F_{rWS}$) and load torque (T) with different $i_d$ and $i_q$.

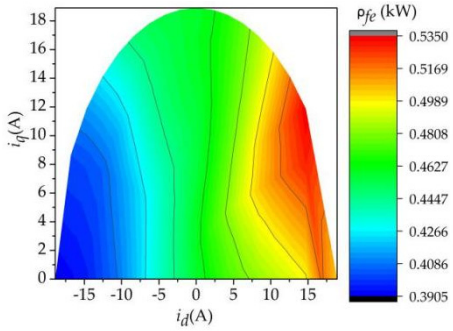


**Figure 17.** The stator iron loss ($\rho_{fe}$) with different $i_d$ and $i_q$.

In addition, the expression of magnetic pull ($F$), load torque ($T_{em}$), and copper loss ($\rho_{cu}$) are shown in (4)–(6), where $f$ is frequency, $K_{dp}$ is winding coefficient, $N$ is the number of series winding turns per phase, $K_\Phi$ is the waveform coefficient of air-gap magnetic flux, $E_0$ is the no-load phase back electromotive force, $X_{ad}$ is the $d$ axis armature reaction reactance, $X_{aq}$ is the $q$ axis armature reaction reactance, $p$ is the number of pole pairs, $\psi_f$ is the magnetic flux linkage of the rotor, $L_d$ is the $d$ axis inductance, $L_q$ the $q$ axis inductance, m is the number of phase, and $R_1$ is the phase resistance.

$$F = \frac{1}{2\mu_0 b L_{ef}} \frac{(E_0 - I_d X_{ad})^2 + (I_q X_{\mathrm{aq}})^2}{\left(4.44 f K_{dp} N K_\phi\right)^2} \tag{4}$$

$$T = p\left[\psi_f i_q + (L_d - L_q) i_d i_q\right] \tag{5}$$

$$\rho_{cu} = m(i_q^2 + i_d^2) R_1 \tag{6}$$

Figures 16 and 17 and expressions (4)–(6) show the following:

(1) The magnetic pull is a function associated to $i_d{}^2$, $i_d$, $i_q{}^2$, and $i_q$, and with the same ($i_d{}^2 + i_q{}^2$) and $i_q$, the absolute value of $F_{rWS}$ with $i_d < 0$ is higher than the absolute value of $F_{rWS}$ with $i_d > 0$;
(2) The load torque is a function associated to $i_q$ and $i_d i_q$, and with same $i_q$, the maximum torque is in the area of $i_d < 0$;
(3) The stator copper loss is a function associated to ($i_d{}^2 + i_q{}^2$);
(4) The stator iron loss is mildly influenced by the current with the same $i$.

Considering the association shown in expressions (4)–(6), the fitted expression of the unbalanced radial magnetic pull of the whole stator ($F_{rWS}$), the average load torque, and

the copper loss are shown in (7)–(9); Figures 18–20 show that the simulation value and fitted value are matched.

$$F_{rWS(k)} = \begin{cases} \begin{pmatrix} -0.02633i_{d(k)}^2 + 2.474i_{d(k)} \\ -0.003863i_{q(k)}^2 + 0.08312i_{q(k)} - 2.534 \end{pmatrix}, \ i_{d(k)} < 0 \\ 0.006319i_{q(k)}^2 - 0.4675i_{q(k)} + 0.731, i_{d(k)} = 0 \\ \begin{pmatrix} -0.03545i_{d(k)}^2 + 2.025i_{d(k)} \\ -0.007533i_{q(k)}^2 - 0.2287i_{q(k)} + 0.1279 \end{pmatrix}, i_{d(k)} > 0 \end{cases} \tag{7}$$

$$T = \begin{cases} 0.5306i_{q(k)} - 0.005427i_{d(k)}i_{q(k)} + 0.1765, \ i_{d(k)} < 0 \\ 0.4963i_{q(k)} + 0.434, i_{d(k)} = 0 \\ \left[0.4981i_{q(k)} - 0.008608i_{d(k)}i_{q(k)} + 0.3892\right], i_{d(k)} > 0 \end{cases} \tag{8}$$

$$\rho_{cu(k)} = 0.003148(i_{q(k)}^2 + i_{d(k)}^2) \tag{9}$$

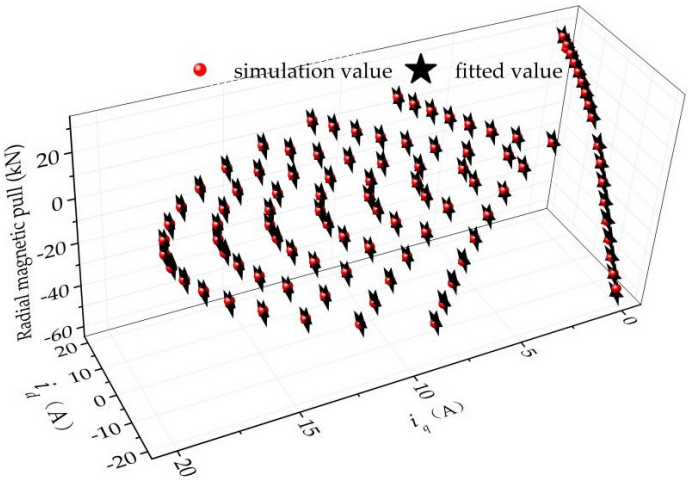


**Figure 18.** Radial magnetic pull of the whole stator ($F_{rWS}$) under different $i_d$ and $i_q$ with one stator module operating.

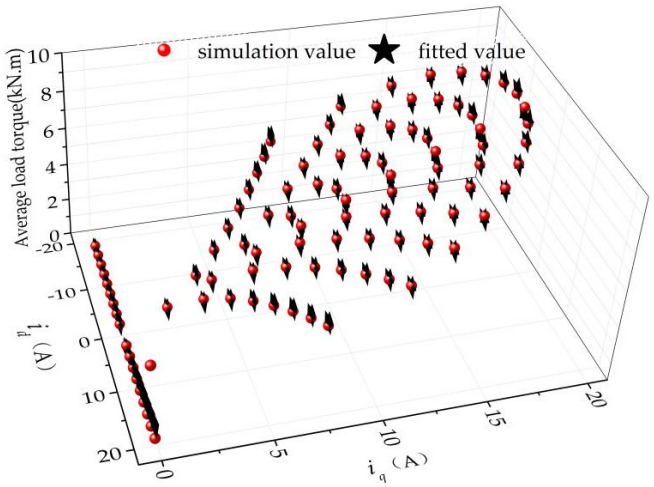


**Figure 19.** The load torque (T) under different $i_d$ and $i_q$ with one stator module operating.

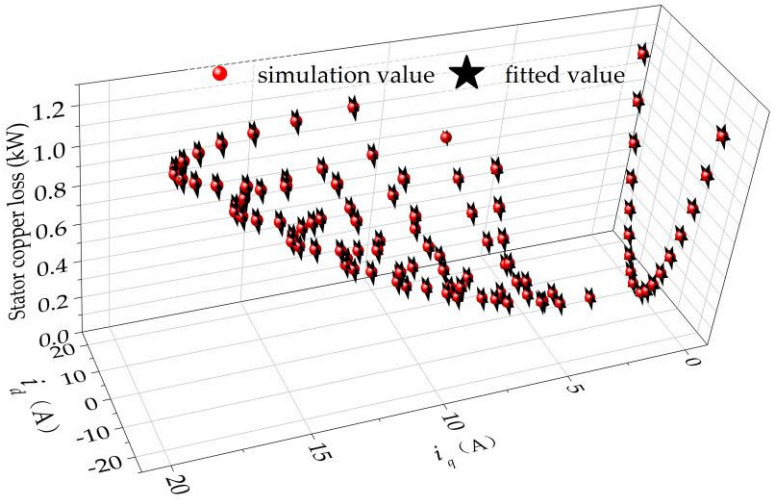


**Figure 20.** The stator copper loss ($\rho_{cu}$) under different $i_d$ and $i_q$ with one stator module operating.

### *5.2. Several Modular Stators Operating*

The combined modular stator operating scheme is classified by the number of modular stators operating. The illustration of the schemes is as follows:

1: a single modular stator operating (for an example, see Figure 21);

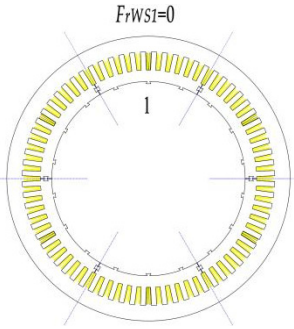


**Figure 21.** Diagrammatic sketch of the combined stator in Scheme 1: the single operating modular stator.

2A: a two-space symmetrical modular stator operating (for an example, see Figure 22a);

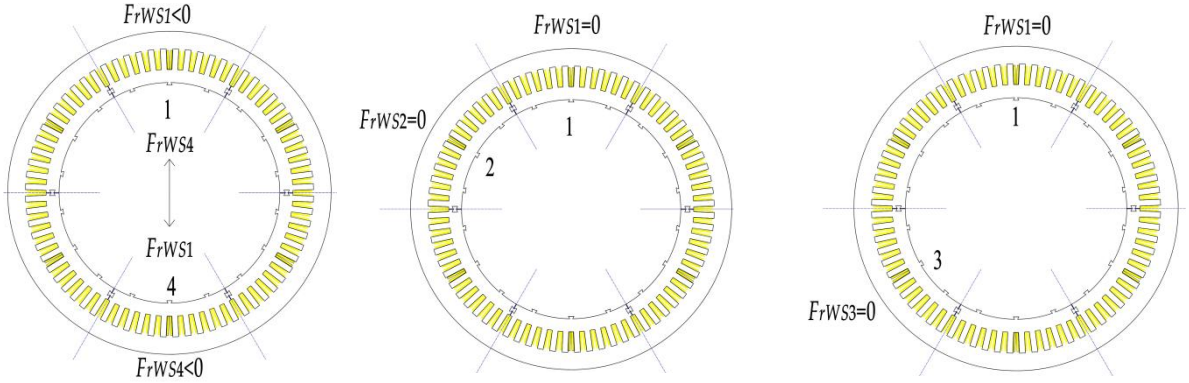


(**a**) Two-space symmetrical modular stator operating (Scheme 2A)

(**b**) Adjacent two-space modular stator operating (Scheme 2B)

(**c**) Two non-adjacent symmetrical space and non-symmetrical space modular stators operating (Scheme 2C)

**Figure 22.** Diagrammatic sketch of combined stators operating in Schemes 2A, 2B, and 2C.

2B: a two-space adjacent modular stator operating (for an example, see Figure 22b);
2C: two modular stators with no adjacent symmetrical spaces and no symmetrical spaces operating (for an example, see Figure 22c);
3A: a three-space symmetrical modular stator operating (for an example, see Figure 23a);

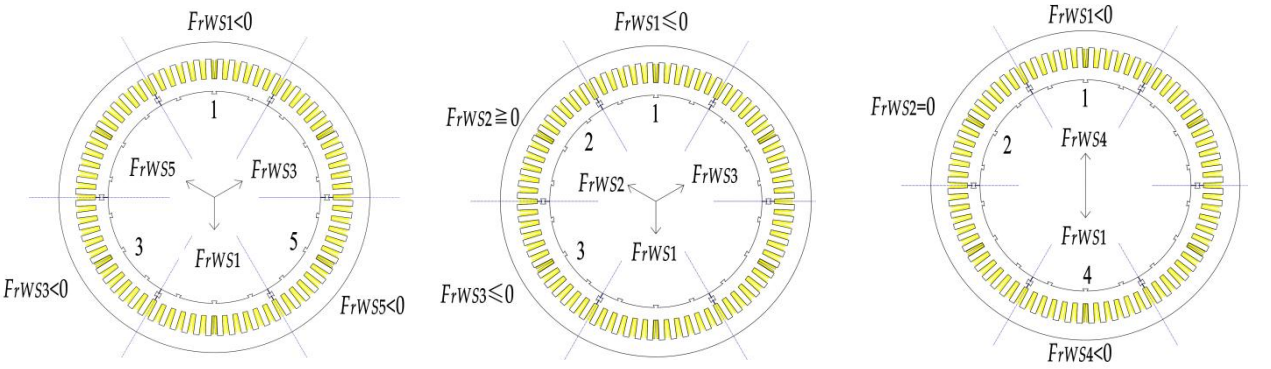


(**a**) Three-space symmetrical modular stator operating (Scheme 3A)

(**b**) Three-space adjacent modular stator operating (Scheme 3B)

(**c**) Three non-adjacent symmetrical space and non-symmetrical space modular stators operating (Scheme 3C)

**Figure 23.** Diagrammatic sketch of combined stators operating in Schemes 3A, 3B and 3C.

3B: a three-space adjacent modular stator operating (for an example, see Figure 23b);
3C: three modular stators with no adjacent symmetrical spaces and no symmetrical spaces operating (for an example, see Figure 23c);
4A: a four-space symmetrical modular stator operating (for an example, see Figure 24a);

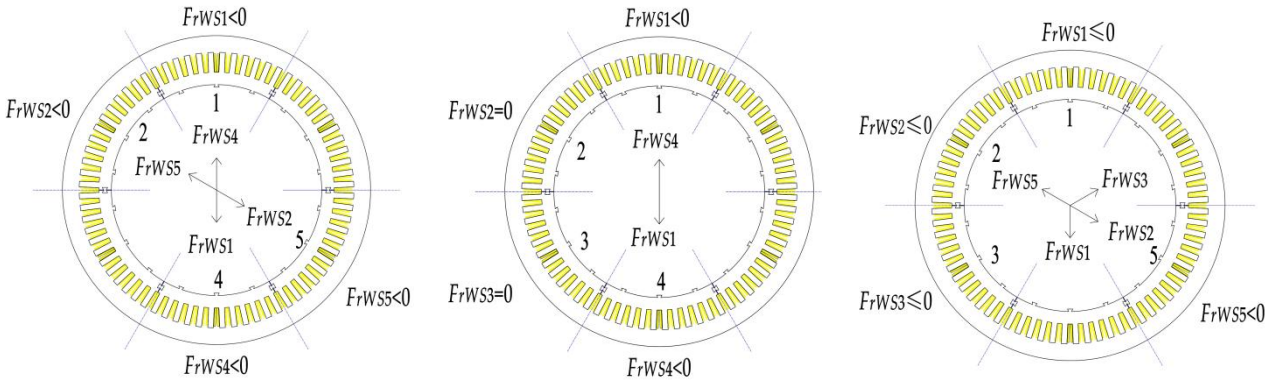


(**a**) Four-space symmetrical modular stator operating (Scheme 4A)

(**b**) Four-space adjacent modular stator operating (Scheme 4B)

(**c**) Four non-adjacent symmetrical space and non-symmetrical space modular stators operating (Scheme 4C)

**Figure 24.** Diagrammatic sketch of combined stators operating in Schemes 4A, 4B, and 4C.

4B: a four-space adjacent modular stator operating (for an example, see Figure 24b);
4C: four modular stators with no adjacent symmetrical spaces and no symmetrical space operating (for an example, see Figure 24c);
5: five modular stators operating (for an example, see Figure 25a);
6: six modular stators operating (for an example, see Figure 25b).
The magnetic pull and current expression for reducing the unbalanced radial magnetic pull of the whole stator ($F_{rWS}$) with different combined stator schemes are shown in Table 2.

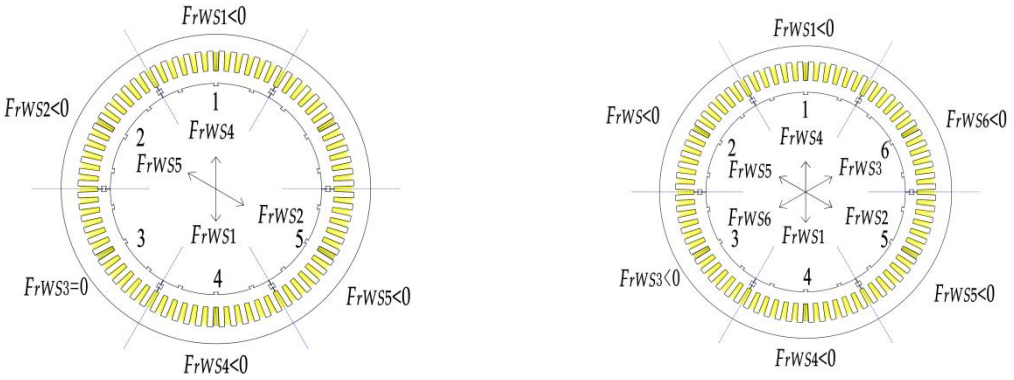


(**a**) Five operating modular stators (Scheme 5) (**b**) Six operating modular stators (Scheme 6)

**Figure 25.** Diagrammatic sketch of combined stators operating in Schemes 5 and 6.

**Table 2.** The magnetic pull and current expression for reducing the unbalanced magnetic pull of the whole stator with different combined stator schemes.

| Combined Operating Stator Scheme Number | Expression |
|---|---|
| 1 | $F_{rWS1} = 0; i_{d1} > 0$ |
| 2A | $F_{rWS1} = F_{rWS4} < 0; i_{d1} = i_{d4} < 0; i_{q1} = i_{q4}$ |
| 2B | $F_{rWS1} = F_{rWS2} = 0; i_{d1} = i_{d2} > 0; i_{q1} = i_{q2}$ |
| 2C | $F_{rWS1} = F_{rWS3} = 0; i_{d1} = i_{d3} > 0; i_{q1} = i_{q3}$ |
| 3A | $F_{rWS1} = F_{rWS3} = F_{rWS5} < 0; i_{d1} = i_{d3} = i_{d5} < 0; i_{q1} = i_{q3} = i_{q5}$ |
| 3B | $F_{rWS1} = F_{rWS3} = -0.5F_{rWS2} \leq 0; F_{rWS2} \geqq 0; i_{d1} = i_{d3} \leq 0; i_{d2} \geqq 0; i_{q1} = i_{q3}$ |
| 3C | $F_{rWS1} = F_{rWS4} < 0; F_{rWS2} = 0; i_{d1} = i_{d4} < 0; i_{d5} > 0; i_{q1} = i_{q4}$ |
| 4A | $F_{rWS1} = F_{rWS2} = F_{rWS4} = F_{rWS5} < 0; i_{d1} = i_{d2} = i_{d4} = i_{d5} < 0; i_{q1} = i_{q2} = i_{q4} = i_{q5}$ |
| 4B | $F_{rWS1} = F_{rWS4} < 0; i_{d1} = i_{d4} < 0; i_{q1} = i_{q4}; F_{rWS2} = F_{rWS3} = 0; i_{d2} = i_{d3} > 0; i_{q2} = i_{q3}$ |
| 4C | $F_{rWS1} + F_{rWS2} = F_{rWS5} < 0; F_{rWS1} = F_{rWS3} \leq 0; i_{d1} = i_{d3} \leq 0; i_{d2} \leq 0; i_{d5} < 0; i_{q1} = i_{q3}$ |
| 5 | $F_{rWS1} = F_{rWS2} = F_{rWS4} = F_{rWS5} < 0; F_{rWS3} = 0;$ $i_{d1} = i_{d2} = i_{d4} = i_{d5} \leq 0; i_{d3} > 0; i_{q1} = i_{q2} = i_{q4} = i_{q5}$ |
| 6 | $F_{rWS1} = F_{rWS2} = F_{rWS3} = F_{rWS4} = F_{rWS5} = F_{rWS6} = 0;$ $i_{d1} = i_{d2} = i_{d3} = i_{d4} = i_{d5} = i_{d6} < 0; i_{q1} = i_{q2} = i_{q3} = i_{q4} = i_{q5} = i_{q6}$ |

When the stator combined number is N, the load torque is assumed to be $T$(N), and the stator copper loss and iron loss are assumed to be $\rho_{cu}$(N) and $\rho_{fe}$(N). Then, the reduction percent of torque is assumed to be $[T(6) - T(\mathrm{N})]/T(6)$, the rising percent of stator copper loss is assumed to be $[\rho_{cu}(\mathrm{N}) - \rho_{cu}(6)]/\rho_{cu}(6)$, and the rising percent of stator copper loss+ iron loss is assumed to be $[\rho_{cu}(\mathrm{N}) + \rho_{fe}(\mathrm{N}) - \rho_{cu}(6) - \rho_{fe}(6)]/[\rho_{cu}(6) + \rho_{fe}(6)]$. Under the premise of $F_{rWS} = 0$, the optimized maximum load torque and loss with different combined operating stator schemes and different phase currents are shown in Figures 26–29. Under the premise of $F_{rWS} = 0$, Figures 26–29 show the following:

(1) With the same whole current ($i_{whole}$) and the same number operating modular stator, sorted by the value of the load torque, the stator combined scheme number is: 2A > 2C > 2B, 3A > 3C > 3B, 4A > 4B > 4C; sorted by the value of core loss, the stator combined scheme number is: 2A < 2C < 2B, 3A < 3C < 3B, 4A < 4B < 4C;

(2) With same whole current ($i_{whole}$), the value of loss is inversely proportional to the number of operating stator modules, especially with respect to copper loss.

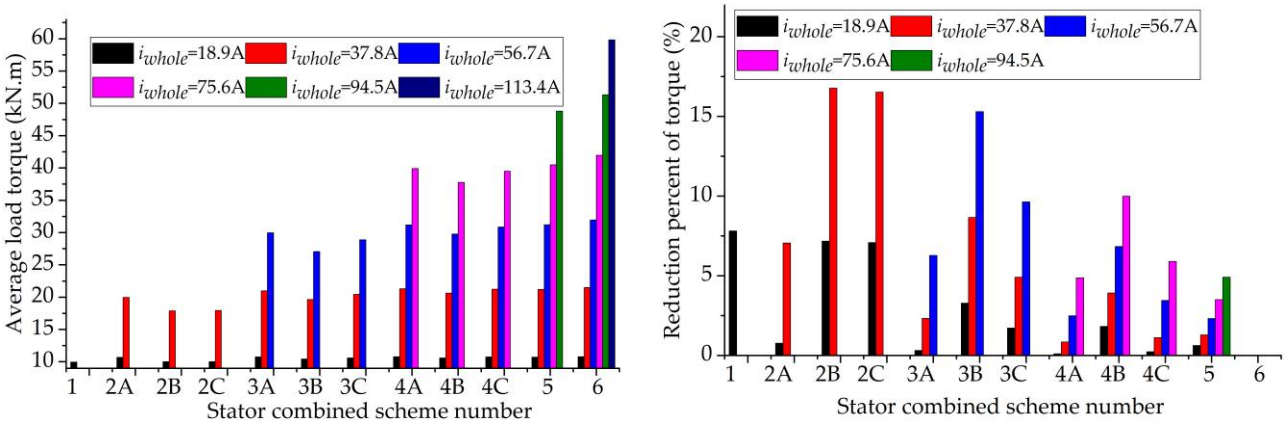


(**a**) Average load torque (**b**) Reduction percent of torque

**Figure 26.** Comparison diagram of load torque with different load currents and different operating modular stator combinations.

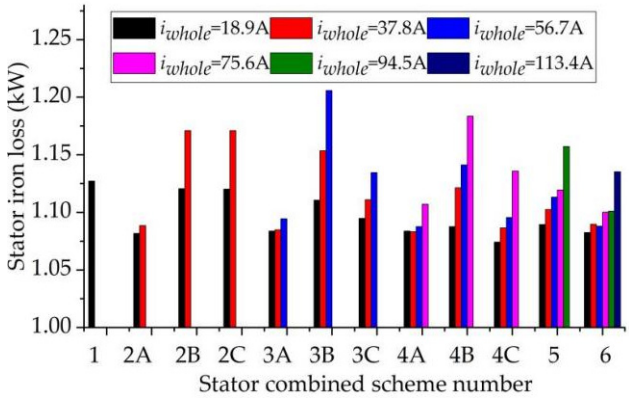


**Figure 27.** Comparison diagram of the iron loss with different load currents and different operating modular stator combinations.

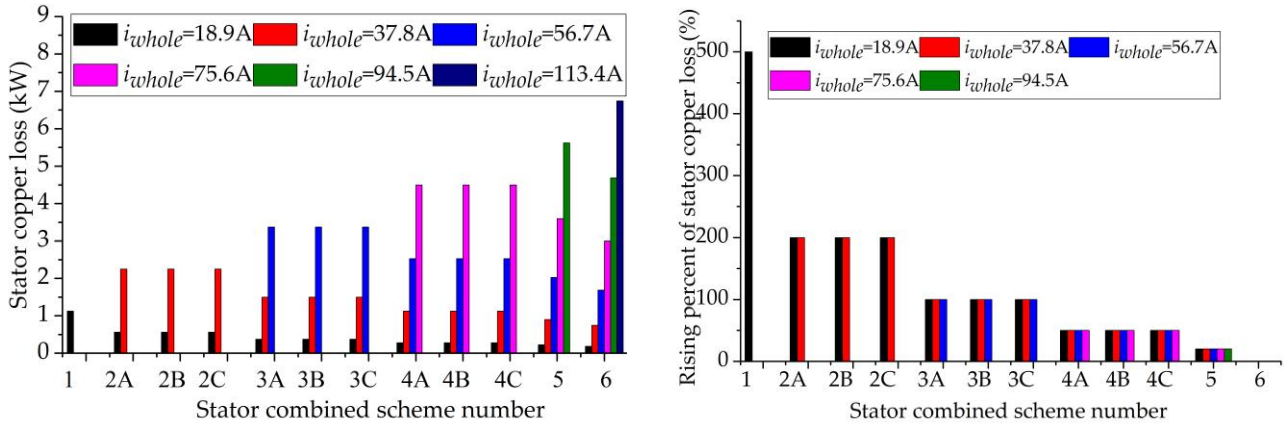


(**a**) Stator copper loss (**b**) Rising percent of stator copper loss

**Figure 28.** Comparison diagram of the copper loss with different load currents and different operating modular stator combinations.

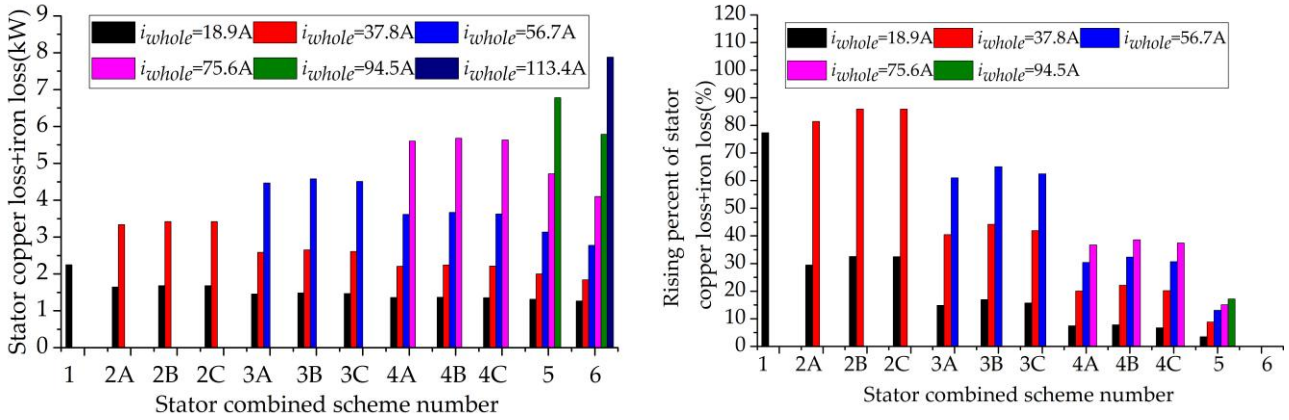


(**a**) Stator copper loss+ iron loss (**b**) Rising percent of stator copper loss

**Figure 29.** Comparison diagram of the stator copper and iron loss with different load currents and different operating modular stator combinations.

## 6. Discussion

This study mainly focused on examining the maximum static of the magnetic pull during the final assembly process of a motor and the dynamic magnetic pull during different motor operating states. New final assembly schemes designed to significantly reduce the static magnetic pull during the motor's final assembly process were proposed, and a method to reduce the unbalanced radial magnetic pull of the whole stator, which is caused by partial stator module operation, was studied.

When the out diameter of the bearings is smaller than the out diameter of the air gap, Scheme A can be used; when the motor is a spoke-type permanent magnet motor and the out diameter of the bearings is smaller than the out diameter of the air gap and rotor, Scheme B can be used. In Scheme B, the value of $F_{WS}$ and $F_{MS}$ with 1.5° radian of magnetic bond can be reduced to 50% value of $F_{WS}$ and $F_{MS}$ with Scheme A; the method to reduce the unbalanced radial magnetic pull of the whole stator, which is caused by part of the stator modules operating, can be used for all modular stator motors with all speeds.

The rotor eccentricity and motor assembly tolerance can also cause an unbalanced magnetic pull. The proposed method to reduce the unbalanced radial magnetic pull of the whole stator can also be influenced by rotor eccentricity and motor assembly tolerance. Therefore, further studies will focus on reducing the unbalanced radial magnetic pull considering rotor eccentricity and motor assembly tolerance.

## 7. Conclusions

The novelty of the paper is:

(1) proposing two assembly scheme for motors, in which the out diameter of bearings is smaller than the out diameter of the air gap, especially in Scheme B for a spoke-type permanent magnet motor.
(2) finding out the maximum static magnetic pull during the motor final assembly process.
(3) a method to reduce the unbalanced radial magnetic pull of the whole stator, which is caused by part of the stator modules operating.

**Author Contributions:** S.S. wrote the paper and implemented simulation; G.F. supervised all processes; B.Z. and Y.L. analyzed the data and checked the paper format. All authors have read and agreed to the published version of the manuscript.

**Funding:** This research received no external funding.

**Data Availability Statement:** Data sharing not applicable.

**Conflicts of Interest:** The authors declare no conflict of interest.

## References


1. Lee, S.G.; Bae, J.; Kim, W.-H. A Study on the Maximum Flux Linkage and the Goodness Factor for the Spoke-Type PMSM. *IEEE Trans. Appl. Supercond.* **2017**, *28*, 1–5. [CrossRef]
2. Ren, X.; Li, D.; Qu, R.; Yu, Z.; Gao, Y. Investigation of Spoke Array Permanent Magnet Vernier Machine with Alternate Flux Bridges. *IEEE Trans. Energy Convers.* **2018**, *33*, 2112–2121. [CrossRef]
3. Sun, L.; Cheng, M.; Tong, M. Key Issues in Design and Manufacture of Magnetic-Geared Dual-Rotor Motor for Hybrid Vehicles. *IEEE Trans. Energy Convers.* **2017**, *32*, 1492–1501. [CrossRef]
4. Jun, C.; Kwon, B. Performance comparison of a spoke-type PM motor with different permanent magnet shapes and the same magnet volume. *IET Electr. Power Appl.* **2017**, *11*, 1196–1204. [CrossRef]
5. Madani, S.; Lipo, T.; Nino, C.; Lugo, D. Modeling of a radial permanent magnet motor with trapezoidal shaped poles. In Proceedings of the IEEE International Conference on Electric Machines and Drives, San Antonio, TX, USA, 15 May 2005; pp. 1715–1719. [CrossRef]
6. Kakihara, W.; Takemoto, M.; Ogasawara, S. Rotor structure in 50 kW spoke-type interior permanent magnet synchronous motor with ferrite permanent magnets for automotive applications. In Proceedings of the 2013 IEEE Energy Conversion Congress and Exposition, Denver, CO, USA, 15–19 September 2013; pp. 606–613. [CrossRef]
7. Boughrara, K.; Ibtiouen, R.; Takorabet, N. Analytic calculation of magnetic field and electromagnetic performances of spoke type IPM topologies with auxiliary magnets. In Proceedings of the 2014 International Conference on Electrical Machines (ICEM), Berlin, Germany, 2–5 September 2014; pp. 51–57.
8. El-Refaie, A.M.; Alexander, J.P.; Galioto, S.; Reddy, P.B.; Huh, K.-K.; de Bock, P.; Shen, X. Advanced High-Power-Density Interior Permanent Magnet Motor for Traction Applications. *IEEE Trans. Ind. Appl.* **2014**, *50*, 3235–3248. [CrossRef]
9. Galioto, S.J.; Reddy, P.B.; El-Refaie, A.M.; Alexander, J.P. Effect of Magnet Types on Performance of High-Speed Spoke Interior-Permanent-Magnet Machines Designed for Traction Applications. *IEEE Trans. Ind. Appl.* **2014**, *51*, 2148–2160. [CrossRef]
10. Kimiabeigi, M.; Mecrow, B.C.; Widmer, J.D.; Long, R.; Gao, Y.; Goss, J.; Martin, R.; Lisle, T.; Vizan, J.M.S.; Michaelides, A. On Selection of Rotor Support Material for a Ferrite Magnet Spoke-Type Traction Motor. *IEEE Trans. Ind. Appl.* **2016**, *52*, 2224–2233. [CrossRef]
11. Yoon, K.-Y.; Kwon, B.-I. Optimal Design of a New Interior Permanent Magnet Motor Using a Flared-Shape Arrangement of Ferrite Magnets. *IEEE Trans. Magn.* **2016**, *52*, 7. [CrossRef]
12. Volpe, G.; Marignetti, F.; Roggia, S.; Popescu, M.; Goss, J. Modified 2-D Model for 3-D Rotor Magnet Leakage Effects in PM Spoke Machines. *IEEE Trans. Ind. Appl.* **2019**, *55*, 3087–3096. [CrossRef]
13. Zhang, H.; Hua, W.; Gerada, D.; Xu, Z.; Gerada, C. Analytical Model of Modular Spoke-Type Permanent Magnet Machines for In-Wheel Traction Applications. *IEEE Trans. Energy Convers.* **2020**, *35*, 1289–1300. [CrossRef]
14. Chen, Q.; Xu, G.; Zhai, F.; Liu, G. A Novel Spoke-Type PM Motor with Auxiliary Salient Poles for Low Torque Pulsation. *IEEE Trans. Ind. Electron.* **2019**, *67*, 4762–4773. [CrossRef]
15. Xiao, Y.; Zhu, Z.Q.; Jewell, G.W.; Chen, J.; Wu, D.; Gong, L. A Novel Spoke-Type Asymmetric Rotor Interior Permanent Magnet Machine. *IEEE Trans. Ind. Appl.* **2021**, *57*, 4840–4851. [CrossRef]
16. Chen, Q.; Xu, G.; Liu, G.; Zhai, F.; Eduku, S. Reduction of Torque Ripple Caused by Slot Harmonics in FSCW Spoke-Type FPM Motors by Assisted Poles. *IEEE Trans. Ind. Electron.* **2019**, *67*, 9613–9622. [CrossRef]
17. Fontana, M.; Bianchi, N. Design and Analysis of Normal Saliency IPM Spoke Motor. *IEEE Trans. Ind. Appl.* **2020**, *56*, 3625–3635. [CrossRef]
18. Nagano, S.; Takemoto, M.; Ogasawara, S. An examination for improvement of constant output characteristics at high-speed region in a spoke-type IPMSM using ferrite permanent magnet by changing the shape of rotor surface. In Proceedings of the 2016 IEEE Energy Conversion Congress and Exposition (ECCE), Milwaukee, WI, USA, 18–22 September 2016; pp. 1–8.
19. Ge, X.; Zhu, Z.Q.; Li, J.; Chen, J. A Spoke-Type IPM Machine with Novel Alternate Airspace Barriers and Reduction of Unipolar Leakage Flux by Step-Staggered Rotor. *IEEE Trans. Ind. Appl.* **2016**, *52*, 4789–4797. [CrossRef]
20. Yoo, J.S.; Jang, H.; Cho, S.; Lee, G.S.; Ko, S.J.; Bae, S.; So, H. Design of rotor with novel barrier for power improvement of spoke-type permanent magnet synchronous motor. In Proceedings of the 2018 21st International Conference on Electrical Machines and Systems (ICEMS), Jeju, Republic of Korea, 7–10 October 2018; pp. 2090–2094.
21. Castano, S.M.; Sayed, E.; Jiang, J.W.; Liang, J.; Bilgin, B.; Sathyan, A.; Emadi, A. Design of a spoke-type ferrite magnet generator for a hybrid electric vehicle application. In Proceedings of the 2019 IEEE Transportation Electrification Conference and Expo (ITEC), Detroit, MI, USA, 19–21 June 2019; pp. 1–6.